http://dx.doi.org/10.1016/j.ultrasmedbio.2013.12.008

ELSEVIER

● *Original Contribution*

ENDOVASCULAR SHEAR STRAIN ELASTOGRAPHY FOR THE DETECTION AND CHARACTERIZATION OF THE SEVERITY OF ATHEROSCLEROTIC PLAQUES: *IN VITRO* VALIDATION AND *IN VIVO* EVALUATION

Younes Majdouline,* Jacques Ohayon,[†‡] Zahra Keshavarz-Motamed,*
Marie-Hélène Roy Cardinal,* Damien Garcia,*[§‖] Louise Allard,* Sophie Lerouge,[¶#]
Frédéric Arsenault,[‖]** Gilles Soulez,[‖]** and Guy Cloutier*[‖]

*Laboratory of Biorheology and Medical Ultrasonics, University of Montreal Hospital Research Center (CRCHUM), Montréal,
Québec, Canada; [†]Laboratory TIMC-IMAG/DyCTiM, University Joseph-Fourier, CNRS UMR 5525, Grenoble, France;
[‡]University of Savoie, Polytech Annecy-Chambery, Le Bourget du Lac, France; [§]Research Unit of Biomechanics and Imaging in
Cardiology, University of Montreal Hospital Research Center (CRCHUM), Montréal, Québec, Canada; [‖]Department of
Radiology, Radio-Oncology and Nuclear Medicine, and Institute of Biomedical Engineering, University of Montreal, Montréal,
Québec, Canada; [¶]Laboratory of Endovascular Biomaterials, University of Montreal Hospital Research Center (CRCHUM),
Montréal, Québec, Canada; [#]Department of Mechanical Engineering, École de technologie supérieure, Montréal, Québec,
Canada; and **Department of Radiology, University of Montreal Hospital (CHUM), Montréal, Québec, Canada

Abstract—This work explores the potential of shear strain elastograms to identify vulnerable atherosclerotic plaques. The Lagrangian speckle model estimator (LSME) elasticity imaging method was further developed to estimate shear strain elasticity (SSE). Three polyvinyl alcohol cryogel vessel phantoms were imaged with an intravascular ultrasound (IVUS) scanner. The estimated SSE maps were validated against finite-element results. Atherosclerosis was induced in carotid arteries of eight Sinclair mini-pigs using a combination of surgical techniques, diabetes and a high-fat diet. IVUS images were acquired *in vivo* in 14 plaques before euthanasia and histology. All plaques were characterized by high magnitudes in SSE maps that correlated with American Heart Association atherosclerosis stage classifications ($r = 0.97$, $p < 0.001$): the worse the plaque condition the higher was the absolute value of SSE, i.e. |SSE| (*e.g.*, mean |SSE| was 3.70 ± 0.40% in Type V plaques, whereas it was reduced to 0.11 ± 0.01% in normal walls). This study indicates the feasibility of using SSE to highlight atherosclerotic plaque vulnerability characteristics. (E-mail: guy.cloutier@umontreal.ca)   © 2014 World Federation for Ultrasound in Medicine & Biology.

Key Words: Vascular elastography, Vulnerable plaques, Shear strain, Atherosclerotic plaque image processing, Swine model, Intravascular ultrasound.

INTRODUCTION

The rupture of a vulnerable atherosclerotic plaque in coronary arteries is recognized as a major cause of acute coronary syndrome (Ambrose et al. 1998; Fuster et al. 2005). Histologic studies have found that vulnerable plaques (*i.e.*, those liable to rupture with thromboembolic complications) are typically characterized by a large extracellular necrotic core, a high inflammatory cell burden and a thin fibrous cap infiltrated by macrophages (Vengrenyuk et al. 2006; Virmani et al. 2006). The histopathology of symptomatic carotid plaques was observed to be equivalent to that of culprit coronary plaques (Redgrave et al. 2006).

Morphologic indicators of vulnerable plaques can be imaged by intravascular ultrasound (IVUS) (Carlier and Tanaka 2006; Rioufol et al. 2002), optical coherence tomography (Jang et al. 2002; Tearney et al. 2008), computed tomography (Fayad et al. 2002) and magnetic resonance imaging (Briley-Saebo et al. 2007). However, because morphologic features are insufficient predictors of risk (Loree et al. 1992; Ohayon et al. 2008), prospective prediction of plaque rupture is still imprecise.

The identification of plaque mechanical and compositional properties is a promising alternative to morphologic

Address correspondence to: Guy Cloutier, Laboratory of Biorheology and Medical Ultrasonics, University of Montreal Hospital Research Center (CRCHUM), Tour Viger (Room R11-464), 900 rue Saint-Denis, Montréal, QC, Canada H2X 0A9. E-mail: guy.cloutier@umontreal.ca

predictors (Finet et al. 2004). In this context, several IVUS-based technologies were developed for the evaluation of vessel lesion characteristics and for therapy planning, namely, endovascular elastography (EVE) (de Korte et al. 2000, 2002), palpography (Céspedes et al. 2000; Schaar et al. 2006) and virtual histology (VH) (Nair et al. 2002, 2007), the latter two methods receiving significant attention. Initial clinical reports on palpography and VH revealed promising study endpoint achievements (Van Mieghem et al. 2006; Serruys et al. 2008). However, these technologies later became controversial with reported high variability (Brugaletta et al. 2012; Frutkin et al. 2007; Murray et al. 2013). At a median follow-up of 3.4 y, palpography for patients with coronary syndromes did not identify fibroatheromas at high risk of rupture or major adverse cardiac events (Brugaletta et al. 2012). VH also failed to properly quantify the necrotic core area, can yield artifact in the presence of calcium and is unable to differentiate a thrombus from a fibrotic or fibrofatty plaque (Maehara et al. 2012; Thim et al. 2010). Combining palpography with VH did not provide any additional information with respect to the identification of fibroatheromas at higher risk of rupture (Brugaletta et al. 2012). Rare technologies aimed at identifying plaque components according to their elasticity modulus (*i.e.,* IVUS modulography) are being developed (Baldewsing et al. 2008; Le Floc'h et al. 2009; Richards and Doyley 2011). The latter technologies still need to be clinically validated. Alternatively for superficial arteries, acoustic radiation force impulse imaging has been proposed, but it also remains to be clinically validated (Allen et al. 2011).

Differences in the stiffness of plaque components may change structural shear stresses (Vito et al. 1990) and, thus, shear strains. Shear failure may also arise at the interface of tissue components with different stiffness (Dickson and Gotlieb 2003; Falk et al. 1995). There is thus increasing evidence supporting the hypothesis that elevated shear strain initiates and/or stimulates the development of a plaque into a plaque liable to rupture (Cinthio et al. 2006; Idzenga et al. 2009, 2012). The shear strain induced in the adventitial layer by the axial movement of the artery may promote the neovascularization of the vasa vasorum, which, in turn, may accelerate plaque progression through intraplaque inflammation and bleeding (Idzenga et al. 2009). Similarly, Lawrence-Brown et al. (2011) hypothesized that shear stresses cause repeated intramural microhemorrhages followed by a healing process leading to plaque development and progression. Identifying shear strain within the arterial wall not only has the potential to improve our knowledge of the properties of the arterial wall in vascular diseases, but also can improve our ability to detect early abnormalities in arterial wall function.

In the context of EVE imaging over a cross section of an artery, early advances relied on intraplaque radial (de Korte et al. 1998; Wan et al. 2001) and circumferential (Liang et al. 2008; Maurice et al. 2008) strain estimates. For a cross-sectional IVUS image, the radial strain corresponds to the deformation along the ultrasound (US) beam, whereas the circumferential strain is orthogonal to it. Shear strain elasticity (SSE) was first reported *in vivo* in three patients with coronary atherosclerotic plaques (Maurice et al. 2007), but according to the new implementation proposed in this study, those results could include artifacts. Indeed, in IVUS imaging, if the transducer is not centered in the artery lumen, US beams are not in the direction of the applied pressure. Therefore, calculated strains along the US beam are not purely radial strains. Few studies have quantified the influence of catheter position on IVUS elastograms (Baldewsing et al. 2004; de Korte et al. 1999; Perrey et al. 2001). De Korte et al. (1999) suggested theoretical functions to correct radial strains for catheter eccentricity or tilt. Their derivation can be applied to non-circular vessel walls as well. Shi et al. (2003, 2005) later derived a more general form of correction for radial strains that included both eccentricity and tilt effects at the same time, but the formulation applies only to cylindrical vessels. To deal with tilt, both of these works relied on prior knowledge of the tilt angle.

The objectives of this study, therefore, were: (i) to further develop EVE based on the Lagrangian speckle model estimator (LSME, which allows estimation of the full 2-D strain tensor) (Maurice et al. 2004) to correctly estimate SSE, and (ii) to present a compensation scheme based on polar coordinate transformations to correct the 2-D strain tensor (*i.e.*, radial strain, circumferential strain and shear strain) for catheter eccentricity. This scheme handles the general geometric shape (not necessarily circular) of the vessels. Because of practicality concerns for 2-D IVUS, this work does not deal with estimating the tilt angle and correcting the strains in that regard.

METHODS

Experimental in vitro study with polyvinyl alcohol cryogel vessel phantoms

Polyvinyl alcohol cryogel (PVA-C) tissue-mimicking material was used to build vascular phantoms. The protocol followed the methodology described elsewhere (Le Floc'h et al. 2010; Maurice et al. 2005). The stiffness of PVA-C increases with the number of freeze-thaw cycles. A temperature-controlled chamber was used to induce solidification and polymerization of PVA-C samples made with a solution of 10% polyvinyl alcohol in pure water. Samples were obtained by one to six 24-h freezing-thawing cycles, with temperatures and

a

b

c
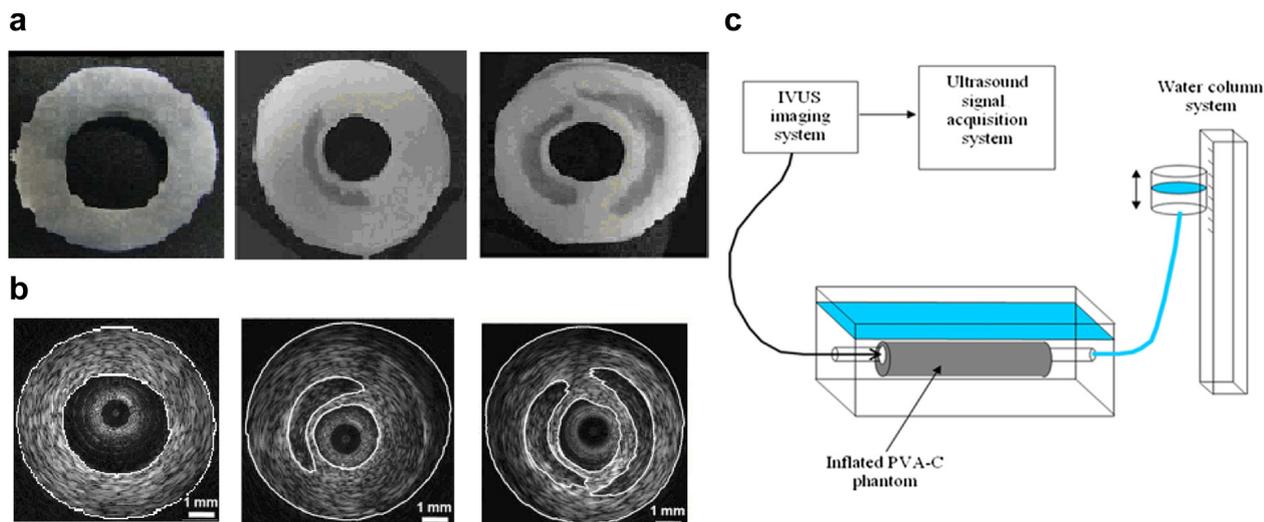
Fig. 1. (a) Sections of two polyvinyl alcohol cryogel (PVA-C) phantoms. (b) Corresponding B-mode intravascular ultrasound (IVUS) images. (c) Diagram of the experimental setup comprising a water tank, the PVA-C phantom, a water column system to pressurize the phantom and the ultrasound acquisition system.

rates of change of $\pm 20\,^{\circ}$C and $\pm 0.2\,^{\circ}$C/min, respectively. Three cylindrical vessel phantoms were made (Fig. 1): one homogeneous, one with a soft inclusion and another with two soft inclusions. The homogeneous vessel phantom underwent one freeze-thaw cycle. The two-composite vessel phantoms experienced six freeze-thaw cycles. Before the last cycle, inclusions mimicking soft necrotic cores were filled with PVA-C undergoing only one freeze-thaw cycle. Simultaneously, similar PVA-C homogeneous cylindrical samples were prepared for mechanical testing using an Eplexor rheometer (Gabo, Ahlden, Germany, load cell of 25 N, sensor sensitivity of 10^{-4} at full range). Young's moduli of the stiff (six freeze-thaw cycles) and soft (one freeze-thaw cycle) PVA-C samples were 145.4 ± 31.8 and 17.6 ± 3.4 kPa, respectively.

A circuit was used to apply quasi-static pressures within arterial phantoms with a water column, as illustrated in Figure 1. During experiments, the water temperature was maintained at $25 \pm 1\,^{\circ}$C. An IVUS scanner (In-Vision Gold, Volcano Therapeutics, Rancho Cordova, CA, USA) equipped with a solid-state 20-MHz catheter (Avanar F/X, Volcano Therapeutics) was used to acquire radiofrequency (RF) signals digitized at 100 MHz with an external data acquisition system (Remora model, Volcano Therapeutics). Cross-sectional RF images were acquired from each phantom at 10 successive pressure steps of 0.5 kPa (*i.e.*, 50 mm of water height) covering the pressure range 0 to 5 kPa.

Finite-element simulations

Pressurization of vessel phantoms was simulated by static finite-element analysis using COMSOL Multiphysics software (Structural Mechanics Module, Version 3.5, COMSOL, Grenoble, France). Plaque geometries were meshed with approximately 1500 six-node triangular elements. Finite-element models were solved under the assumption of plane strains. For each vessel phantom, 10 successive pressure steps were imposed, corresponding to pressure increases from 0 to 5 kPa. A free boundary condition was assumed on the external contour of the arteries, and pressure was applied on the lumen boundary. The stiff (mimicking fibrosis) and soft (mimicking lipid) PVA-C phantom components were modeled as isotropic and quasi-incompressible (Poisson's ratio = 0.49), with Young's moduli $E_{\text{fibrosis}} = 145$ kPa and $E_{\text{lipid}} = 17$ kPa, as experimentally determined (Le Floc'h et al. 2010).

Animal experiments

A complete description of animal preparation and measurements can be found in Soulez et al. (2012); only a brief summary is provided here. Protocols for animal experiments were approved by the animal care committee of the Centre Hospitalier de l'Université de Montreal. Eight Sinclair male mini-pigs (Sinclair Research Center, Auxvasse, MO, USA) with a mean age of 211 ± 36 d and mean weight of 35 ± 8 kg at the beginning of the protocol were included in this study. Common carotid arteries were partially ligated with a 1.3-mm spacer on the external surface of the vessel, 4 cm below the carotid bifurcation (Ishii et al. 2006). Removing the spacer before closing the incision resulted in 70%–80% stenosis. The carotid on each side of the neck was randomly ligated with a permanent or an absorbable suture, the latter promoting inflammation. One week after surgery, a 4-F Glidecath catheter (Terumo, Tokyo, Japan) was inserted through a femoral approach to induce diabetes by selective injection of
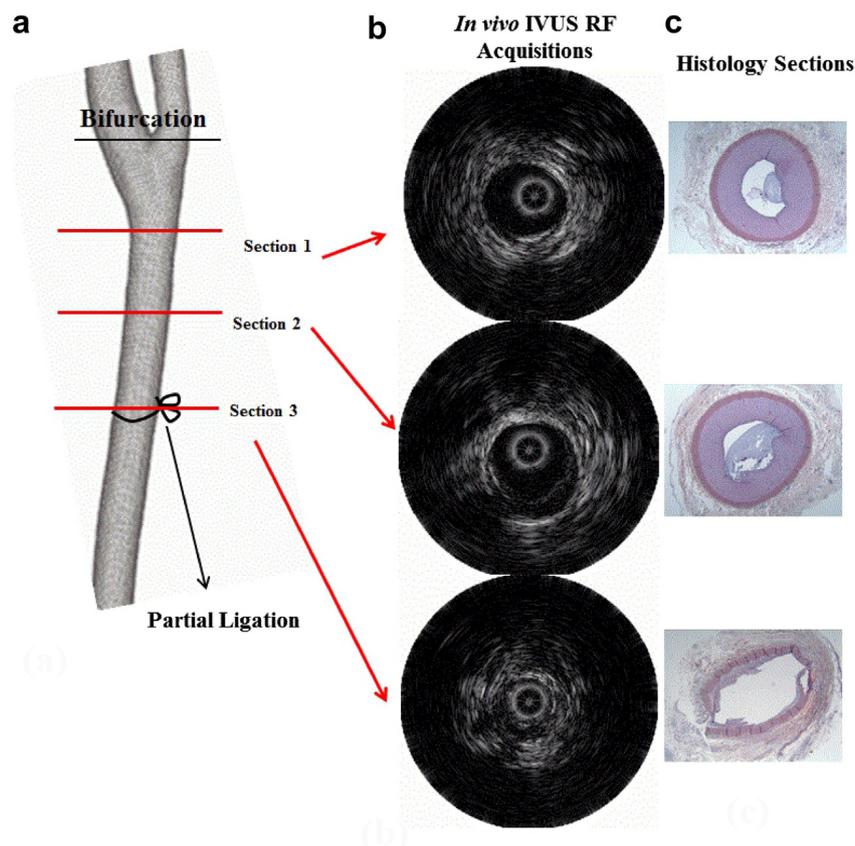
Fig. 2. Schematic of the image acquisition protocol. (a) Different sections with respect to the position of the partial ligation of common carotid arteries. (b) B-mode intravascular ultrasound (IVUS) images reconstructed from radiofrequency (RF) data. (c) Histology sections.

streptozotocin into splenic and gastroduodenal arteries (120 mg/kg). One week after diabetes induction, a high-fat, high-cholesterol diet (TD.96366 Swine High Fat Diet, Harlan Teklad, Madison, WI, USA) was started to induce hypercholesterolemia, and lasted 20 wk, at which point animals were euthanized.

Angiography of both carotid arteries was performed through a femoral approach with a 4-F Glide-cath catheter (Terumo) before euthanasia, to grade the severity of stenoses in diameter reduction. Mild to severe carotid stenoses were observed (stenosis severity = $80.4 \pm 12.4\%$ with permanent sutures and $48.8 \pm 39.0\%$ with absorbable sutures). Permanent sutures resulted in more advanced atherosclerotic lesions (Soulez et al. 2012). Under fluoroscopy guidance, IVUS pullback scans were done on both carotid arteries using an automatic positioning system set at 0.5 mm/s. IVUS B-mode images were acquired with a 3.5-F 20-MHz probe (Avanar F/X, Volcano Therapeutics) at a frame rate of 30/s. Then, atherosclerotic plaques of interest were imaged again with static positioning of the IVUS catheter along the artery to acquire RF data of the pulsating vessel. The exact position of the IVUS catheter tip was identified under fluoroscopy and the distance from the carotid bifurcation was noted. As reported earlier (Soulez et al. 2012), we observed atherosclerotic lesions upstream and downstream of the ligation site (see Fig. 2 for a schematic of the image acquisition protocol).

Histologic analyses

To prepare carotid arteries for sectioning, they were perfused with saline for 5 min followed by 10% buffered formalin at 150 mm Hg for 1 h. For every 5 mm of specimens, sections 6 μm thick were made. Additional serial sections were collected when a plaque was detected. Three stains were employed: (i) Hematoxylin phloxine saffron stain was used to differentiate collagen (yellow), nuclei (blue) and muscle or cytoplasm (pink). (ii) Movat stain was chosen to differentiate elastic fibers (black), collagen (yellow-green), nuclei (dark blue), cytoplasm (pink-brown) and calcium (brown). (iii) If Movat staining suggested the presence of calcium, a more quantitative von Kossa stain was employed to highlight calcium nodules in black. Picrosirius red stain was also used for collagen and lipid analyses. A pathologist blinded to

Table 1. American Heart Association classification of atherosclerotic lesions

Lesion type	Description
I	Initial lesion with foam cells (intimal xanthoma or fatty streak)
II	Fatty streak with multiple foam cell layers
III	Pre-atheroma with extracellular lipid pools
IV	Atheroma with a confluent extracellular lipid core
V	Fibro-atheroma
VI	Complex plaque with possible surface defect or hemorrhage or thrombus or some combination
VII	Calcified plaque
VIII	Fibrotic plaque without lipid core

the location or type of suture classified plaques according to the American Heart Association (AHA) atherosclerosis stage classification (Table 1), which summarizes the natural history of atherosclerosis (Soulez et al. 2012; Stary 2000). An in-house semi-automatic segmentation method developed in MATLAB (Version 6.5. The MathWorks, Natick, MA, USA) and adapted to ImageJ software (National Institutes of Health open source, Bethesda, MD, USA) was used for histomorphometric analyses.

Registration between radiofrequency data and histology

As mentioned above, IVUS scanning of the left and right carotid vessels was performed under angiography guidance to identify sites with stenoses. IVUS scanning was started at the bifurcation junction and then repeated eight times at spatial steps of 1 cm below the junction along the vessel. The specific scan in which the plaque appeared was used for further analysis. The histology slice used for validation was the slice at the same location of the scan. Because the initial (on removal from the body) and final (before slicing) lengths of the vessel were known, tissue shrinkage was calculated to locate the correct position of the slice. Registration between RF data and histology was done using the location of the plaque identified by a radiologist before performing elastographic calculations.

Plaque strain reconstruction

Image segmentation. IVUS reconstructed B-mode images (from acquired RF data with Hilbert transformation and logarithm compression) were segmented to detect the lumen boundary using a fast-marching model combining region and contour information (Roy Cardinal et al. 2006). The outer contour was computed by shifting the detected lumen boundary outwardly by a distance of 1 mm radially. Resulting contours were validated by a radiologist (G.S.) before further processing. Remaining analyses were done on a region of interest

(ROI) that included the artery wall, as defined by the area between the lumen boundary and the outer contour. The ROI included some portion or the entire plaque area, as well as normal regions of the vessel wall.

LSME elastography algorithm. The LSME method was described in detail elsewhere (Maurice et al. 2004). We provide a succinct description herein that will help in understanding the new implementation described in Appendix A.

In the context of EVE, we aimed to find components of the strain tensor within the artery wall. Consequently, displacements at any locations, as well as their spatial derivatives, are required. For this purpose, the LSME was adapted to process RF IVUS data in the polar coordinate system.

Radiofrequency images were first registered to compensate for rigid motion caused by catheter movement artifacts. For this purpose, overlapping measurement windows (MWs) within ROIs of two consecutive temporal images were analyzed. For each MW, 2-D correlation coefficients between images were calculated, and the motion of the catheter was determined as the shifts of the maximum correlation point.

The second temporal image was then compensated for this translation artifact. At each point within a MW, the optical flow equation in polar coordinates was expanded around the center of the MW (M_0), using Taylor series, making an over-determined system of equations in terms of the optical flow components and their partial spatial derivatives. The least-squares solution of this system of equations was obtained. The 2-D displacement gradient matrix (Δ) in polar coordinate can be defined as

$$\Delta = \begin{bmatrix} \Delta_{rr} & \Delta_{r\theta} \\ \Delta_{\theta r} & \Delta_{\theta\theta} \end{bmatrix} = \begin{bmatrix} \frac{\partial U_r}{\partial r} & \frac{1}{r}\left(\frac{\partial U_r}{\partial \theta} - U_\theta\right) \\ \frac{\partial U_\theta}{\partial r} & \frac{1}{r}\left(\frac{\partial U_\theta}{\partial \theta} + U_r\right) \end{bmatrix} \quad (1)$$

Components of the strain tensor in polar coordinates $\varepsilon_{ij} = \frac{1}{2}(\Delta_{ij} + \Delta_{ji})$ can be calculated as

$$\varepsilon = \begin{bmatrix} \varepsilon_{rr} & \varepsilon_{r\theta} \\ \varepsilon_{\theta r} & \varepsilon_{\theta\theta} \end{bmatrix} = \begin{bmatrix} \Delta_{rr} & \frac{1}{2}(\Delta_{r\theta} + \Delta_{\theta r}) \\ \frac{1}{2}(\Delta_{r\theta} + \Delta_{\theta r}) & \Delta_{\theta\theta} \end{bmatrix} \quad (2)$$

Here, Δ, ε and U are the displacement gradient tensor, strain tensor and displacement vector, respectively. In this work, because of the known variability in estimating lateral strains with US elastography methods, only one component of the shear strain ($\Delta_{r\theta}$) was investigated and validated against experimental data. More details about calculating displacement gradient tensors based on the above description are reported in Appendix A.

In this study, sizes of 2-D MWs were 120 lines and 30 sample points (0.924 mm × 0.48 radian), with 90%
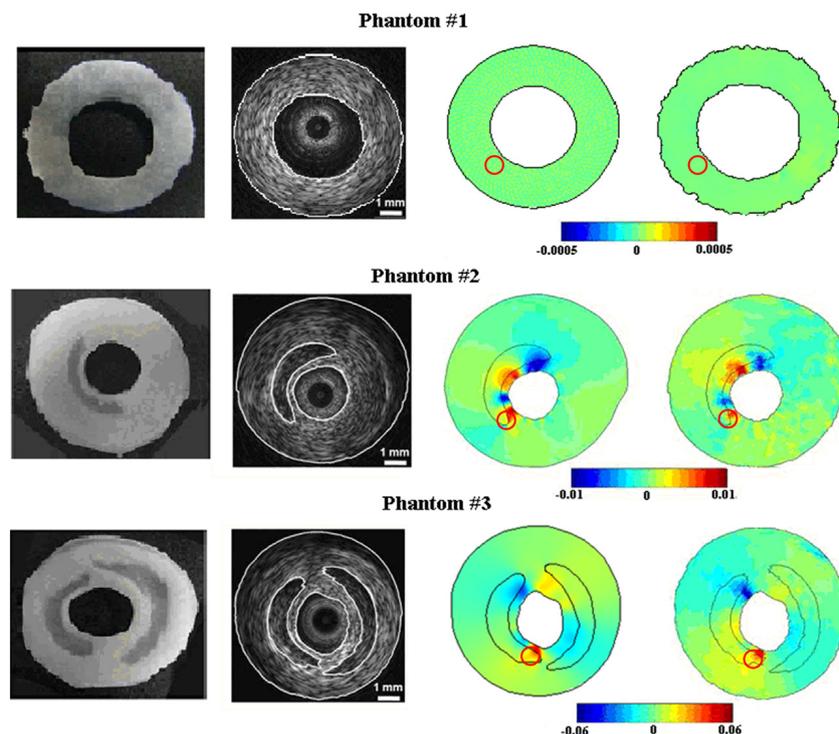
Fig. 3. Performance of the Lagrangian speckle model estimator (LSME) in quantifying shear strain elasticity (SSE) using experimental intravascular ultrasound (IVUS) images acquired on three polyvinyl alcohol cryogel (PVA-C) phantoms. *First column*: Sections of three PVA-C vascular phantoms. *Second column*: Segmented B-mode IVUS images reconstructed from radiofrequency data. *Third column*: Reference SSE map simulated by finite-element modeling. *Fourth column*: Estimated SSE map obtained with the LSME. The *red circle* on each SSE panel indicates a region of quantitative comparisons (see Fig. 4).

radial and circumferential overlaps. Each SSE map was calculated based on a pair of consecutive RF data (phantom: 512 lines and 1120 sample points; mini-pig: 512 lines and 800 sample points). For phantom experiments, the reported SSE maps were arbitrarily chosen at a given pressure from 0 to 5 kPa, whereas for the pig study, SSE maps were obtained during diastole. SSE maps were smoothed using a 5×5 median filter padded with symmetric expansion at the boundaries. For display purposes, *in vivo* SSE maps were zoomed in so they had different dimension scales compared with their respecting IVUS images (see the caption of Fig. 5).

Compensation for the eccentricity of the catheter. One issue limiting the performance of IVUS elastography is the eccentricity of the catheter within the vessel lumen, caused by pulsatile flow and cardiac motion, potentially leading to erroneous strain estimates from geometric artifacts. Compensating for the eccentric catheter position (Baldewsing et al. 2004; de Korte et al. 1999; Perrey et al. 2001; Shi et al. 2003, 2005) is a challenging task in IVUS elastography. In this study, a method was developed to estimate the eccentricity and to correct the strains in the polar coordinate system. Unlike previously suggested methods, our approach

does not assume sole radial motion as in Shapo et al. (1996) and corrects the complete strain tensor without any restricting assumptions on the vessel morphology. Details and complete equations of the method are reported in Appendix B.

Statistical analyses

Results were expressed as means $\pm$ standard deviations (SD). Statistical analyses were performed using SigmaStat software (Version 3.1, Systat Software, San Jose, CA, USA). Analyses of variance and Pearson correlations were performed to detect any significant relation between SSE and AHA classifications of atherosclerotic lesions. One-way analysis of variance was used to compare SSE results for plaques with those for normal vessel walls.

RESULTS

Shear strains are amplified in the mimicked thin-cap fibroatheroma

Figure 3 illustrates the performance of the new LSME implementation to estimate SSE and its reliability by comparing results with finite-element simulations. All three investigated cases are included in this figure: a
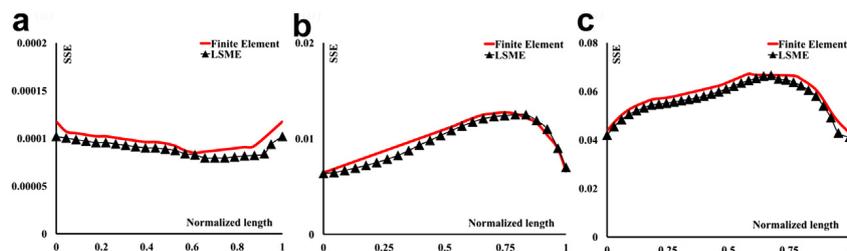
Fig. 4. Shear strain elasticity (SSE) along the line outlined by the red circles in Figure 3 for (a) phantom 1 (homogeneous), (b) phantom 2 (with a soft inclusion) and (c) phantom 3 (with two soft inclusions). LSME = Lagrangian speckle model estimator.

mimicked normal vessel wall and plaques with one or two soft inclusions. In all cases, results exhibit very good qualitative agreements between reference shear strains computed using the finite-element method and estimated shear strain elastograms. Quantitatively, there was also very good agreement between simulated and experimental SSE values along circular lines (*red circles* in Fig. 3), with root-mean-square errors of 0.87% for the normal vessel, 1.35% for the single-soft-inclusion phantom and 1.90% for the double-soft-inclusion mimicked artery (Fig. 4).

The homogeneous phantom did not display any regions of elevated SSE (shear strain values are close to zero, see Fig. 3, first row). The regions of high shear strain in one-inclusion (Fig. 3, second row) and two-inclusion (Fig. 3, third row) phantoms are located at the mimicked thin fibrous cap positions. As an example, in the two-inclusion phantom (#3), the SSE magnitude in the right half ($\approx +0.01$ to -0.01 for positive and negative shear strain values, respectively) is lower than that (≈ 0.06 to -0.04 for positive and negative shear strain

values, respectively) in the left half. These lower SSE values for the right inclusion might be due to the difference in cap thicknesses.

Higher shear strains coincide with plaque locations in vivo

Fourteen carotid plaques were harvested from the eight atherosclerotic pigs (Table 2). The estimated SSE maps calculated from *in vivo* RF data with the new LSME development were compared with histologic observations (Fig. 5). Figure 5 reveals overall good agreement between regions of high SSE (middle column) and histologic plaque locations (right column). This figure reveals the estimated SSE in a few typical examples in which intensified SSE magnitudes in plaque areas can be observed. Normal parts of vascular walls (parts of the vessel wall without any pathologic lesion) typically have low SSE values.

Magnitude of SSE increases with AHA atherosclerotic plaque class

Strong correlations between AHA classes of atherosclerotic lesions and mean (or max) absolute value of SSE, i.e. |SSE|, computed over the entire vessel wall cross section were found: $r = 0.97$, $p < 0.001$ for mean |SSE|, and $r = 0.93$, $p < 0.001$ for max |SSE| (Fig. 6). Table 3 illustrates the correspondence between AHA class and SSE value for data collected in the present study. This table indicates that the worse the plaque condition (in terms of histopathology analysis), the higher are the mean and maximum |SSE|. Table 3 also lists ratios of mean and maximum |SSE| values in plaques to those in normal vessel walls. Those ratios follow the same trend as AHA classes. As an example, for Type V plaques, mean |SSE| was $3.70 \pm 0.40\%$ and max |SSE| was $7.37 \pm 0.36\%$. On the other hand, in normal regions of carotid arteries, |SSE| values were significantly decreased, with mean and maximum values reduced to $0.11 \pm 0.01\%$ and $0.19 \pm 0.01\%$, respectively. The third column in Table 3, which gives mean |SSE| values normalized by the pressure gradient measured with a catheter within the femoral artery of

Table 2. Data on carotid plaques from eight atherosclerotic pigs

Plaque no./pig no.	Severity of stenosis	Side of carotid	AHA atherosclerosis stage classification/stain used	Plaque location
1/1	75%	Right	Type I/HPS	3 cm below bifurcation
2/1	42%	Left	Type I/Movat	4 cm below bifurcation
3/2	73%	Right	Type II/Movat	At bifurcation
4/3	95%	Right	Type II/Movat	3 cm below bifurcation
5/3	90%	Left	Type III/Movat	4 cm below bifurcation
6/3	90%	Left	Type III/Movat	5 cm below bifurcation
7/4	71%	Right	Type IV/HPS	4 cm below bifurcation
8/5	80%	Right	Type IV/Movat	2 cm below bifurcation
9/5	80%	Right	Type IV/Movat	3 cm below bifurcation
10/6	80%	Right	Type IV/HPS	7 cm below bifurcation
11/7	64%	Right	Type V/Movat	7 cm below bifurcation
12/7	64%	Right	Type V/Movat	8 cm below bifurcation
13/8	95%	Right	Type V/Movat	3 cm below bifurcation
14/8	95%	Left	Type V/HPS	4 cm below bifurcation

AHA = American Heart Association; HPS = hematoxylin phloxine saffron.
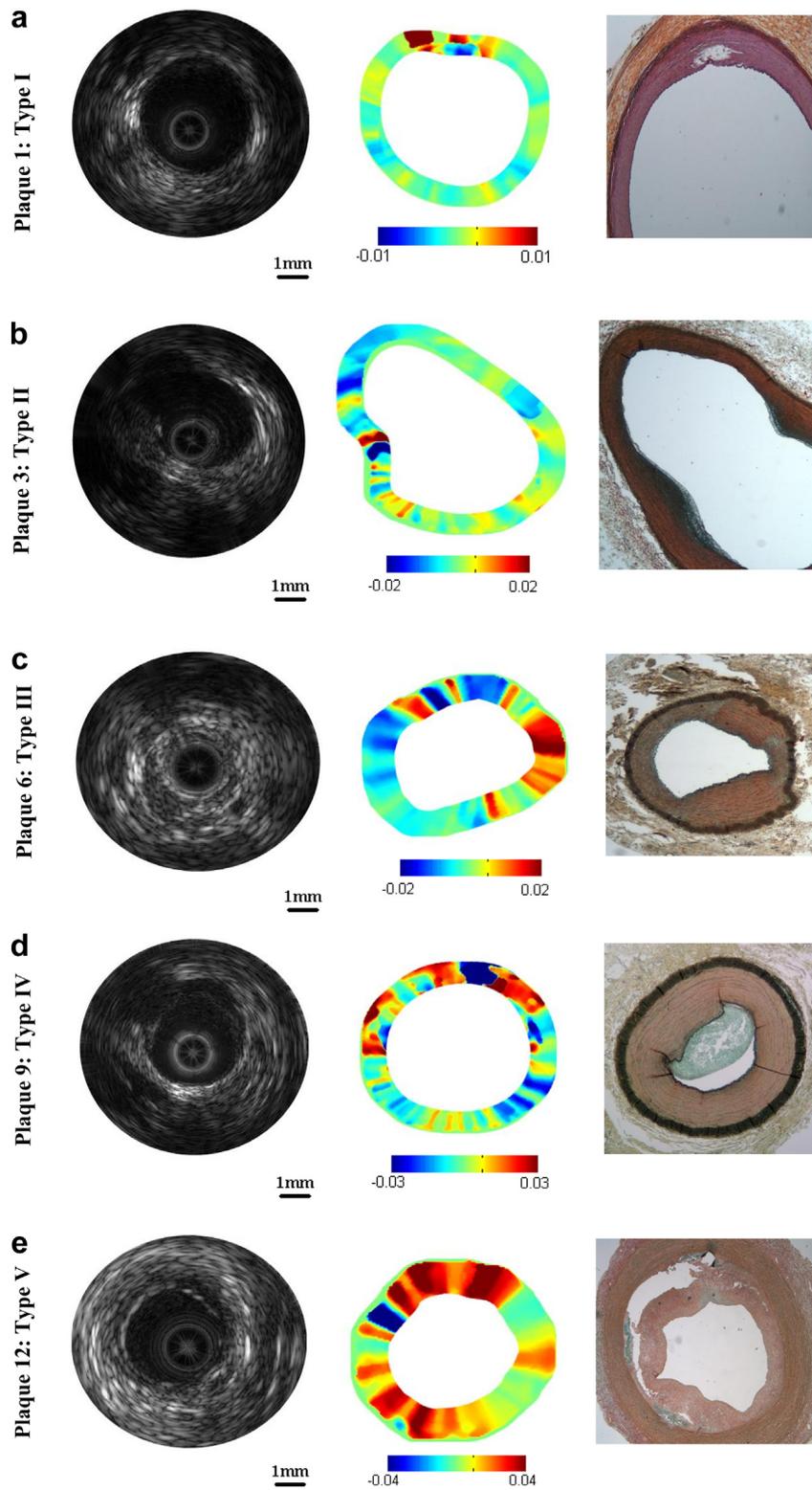
Fig. 5. *Left column*: *In vivo* intravascular ultrasound images. *Middle column*: Estimated shear strain elasticity (SSE) maps. *Right column*: Histologic stained samples of excised lesions for which SSE was obtained. SSE maps (*middle*) were calculated with the RF data used to produce the B-mode image of the first column. For better visualization, the SSE map was zoomed with respect to its B-mode image (by 145%). Note that higher shear strains coincide with plaque location. American Heart Association class: (a) Type I, (b) Type II, (c) Type III, (d) Type IV, (e) Type V.
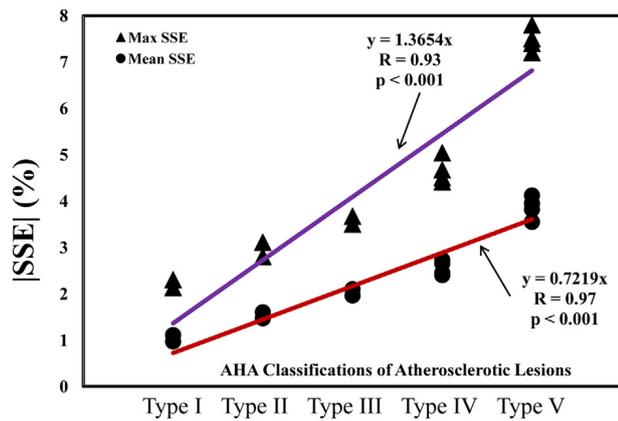
Fig. 6. Analyses of correlations between mean and max estimated |SSE| and American Heart Association classification of atherosclerotic lesions. SSE = shear strain elasticity.

value by the measured pressure gradient. For all animals, the mean systolic pressure was 106 ± 20 mm Hg and the mean diastolic pressure was 65 ± 18 mm Hg. Figure 7 illustrates correlations between AHA atherosclerotic lesion class and mean (or max) |SSE| values normalized by the pressure gradient: $r = 0.96$, $p < 0.001$ for mean |SSE|, and $r = 0.95$, $p < 0.001$ for max |SSE|.

DISCUSSION

From a biomechanical point of view, elevated shear strain is increasingly being considered an important factor for initiating and/or stimulating the development of a plaque into a plaque likely to rupture by cap weakening leading to ulceration (Cinthio et al. 2006; Idzenga et al. 2009; 2012). Accurate estimation of the shear strain is also imperative for *in vivo* quantification of both the morphology and mechanical properties of a diseased artery at any given instant of the remodeling process.

each animal, confirms this trend and eliminates the potential confounding impact of this factor on results. The normalized |SSE| was obtained by dividing its

Table 3. Analyses of correlations between estimated |SSE| and AHA atherosclerosis stage (n = 14)

AHA class	Mean and max |SSE| (%)	Mean |SSE| (%) normalized by pressure gradient (mm Hg^{-1})	Ratio of mean/max |SSE| to those in normal vessel wall
Type I (n = 2)	**Mean***: Min = 0.81; Max: 0.96 $N = 7$ $^\ddagger p < 0.001$, $^\S p < 0.001$ **Max**†: Min = 1.84, Max = 2.26 $N = 7$ $^\ddagger p < 0.001$, $^\S p < 0.01$	**Mean***: Min = 0.020; Max = 0.024 $^\ddagger p < 0.01$, $^\S p < 0.05$	8/11
Type II (n = 2)	**Mean***: Min = 1.38, Max = 1.57 $N = 7$ $^\ddagger p < 0.05$; $^\S p < 0.01$ **Max**†: Min = 2.77, Max = 3.01 $N = 8$ $^\ddagger p < 0.05$, $^\S p < 0.05$	**Mean***: Min = 0.038; Max = 0.042 $^\ddagger p < 0.001$, $^\S p < 0.01$	14/15
Type III (n = 2)	**Mean***: Min = 1.87, Max = 2.22 $N = 7$ $^\ddagger p < 0.05$, $^\S p < 0.01$ **Max**†: Min = 3.41, Max = 3.75 $N = 7$ $^\ddagger p < 0.05$, $^\S p < 0.01$	**Mean***: Min = 0.047, Max = 0.055 $^\ddagger p < 0.05$, $^\S p < 0.01$	18/19
Type IV (n = 4)	**Mean***: Min = 2.17, Max = 2.5 $N = 4$ $^\ddagger p < 0.05$, $^\S p < 0.01$ **Max**†: Min = 4.4, Max = 5.1 $N = 4$ $^\ddagger p < 0.05$, $^\S p < 0.05$	**Mean***: Min = 0.062, Max = 0.071 $^\ddagger p < 0.01$, $^\S p < 0.001$	21/24
Type V (n = 4)	**Mean***: Min = 3.3, Max = 4.34 $N = 5$ $^\ddagger p < 0.001$, $^\S p < 0.001$ **Max**†: Min = 6.9, Max = 7.9 $N = 5$ $^\ddagger p < 0.001$, $^\S p < 0.001$	**Mean***: Min = 0.08, Max = 0.1 $^\ddagger p < 0.01$, $^\S p < 0.05$	33/38
Normal wall (n = 14)	**Mean***: Min = 0.1, Max = 0.13 $N = 8$ **Max**†: Min = 0.16, Max = 0.21 $N = 8$	**Mean***: Min = 0.003, Max = 0.0036 $^\ddagger p < 0.001$, $^\S p < 0.001$	

SSE = shear strain elasticity; AHA = American Heart Association; N = required minimum population of plaques with 95% confidence.
* Mean |SSE| computed over vessel wall cross section.
† Max |SSE| computed over vessel wall cross section.
‡ Compared with normal wall.
§ Compared with all other types of atherosclerosis class.
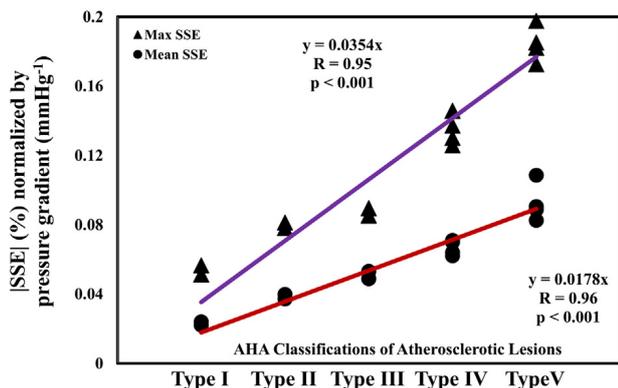
Fig. 7. Analyses of correlations between mean and max estimated |SSE|, normalized by the pressure gradient measured with a catheter within the femoral artery of each animal, and American Heart Association classification of atherosclerotic lesions.

The morphology and mechanical properties are crucial for prediction of plaque rupture (Cheng et al. 1993; Finet et al. 2004) and may also guide the development of specific therapies for prevention of acute events.

The most important findings of the present study are as follows:

1. Stary (2000) recommended the AHA atherosclerosis stage classification to convey results of an inquiry into compositions of atherosclerotic lesions as they silently develop. Results of the present study indicated a link between estimated SSE and AHA atherosclerosis class. We observed that the absolute value of SSE was statistically higher in plaques in higher AHA classes and, therefore, with higher vulnerability. This correspondence needs to be further investigated with larger samples and preferably in humans.

2. Results also revealed that areas with elevated |SSE| values may be used to detect plaque locations. In addition, normal parts of the vascular wall had much lower SSE values. Therefore, the SSE-enabled LSME technique may have the potential to localize and identify plaque features *in vivo*.

3. Our results suggest that SSE may allow evaluation of the thin-cap fibroatheroma stress amplitude, which appears to be a good biomechanical predictor of plaque rupture (Ohayon et al. 2008).

Potential clinical implications

The data presented in this study were based on a rather small population with data acquired in a pig model. However, the aforementioned results indicate the potential for integration of SSE into clinical practice for early evaluation of atherosclerotic plaques before they become vulnerable. More specifically, the following issues can be considered:

1. The *in vivo* quantification of mechanical properties of vulnerable plaque components at any given instant of the remodeling process remains a major issue. It could lead to the development of specific therapies for prevention of acute coronary events (Cheng et al. 1993; Finet et al. 2004; Libby 2001). Supplementing conventional IVUS elastograms with SSE maps may help in improving the accuracy of *in vivo* quantification of plaque mechanical properties. However, this needs to be assessed in humans and to be clinically validated afterward.

2. Our *in vivo* data suggest that high shear strains are linked to AHA atherosclerosis class and, therefore, may become a potential quantity for predicting future events. Therefore, supplementing the current clinical procedure with SSE can be useful to identify patients who are at a high risk and in need of closer follow-up and further investigation, as well as to improve risk stratification and clinical decision making.

3. It is recognized that a very small structural change in a vulnerable plaque can change its stability (Le'Floch et al. 2010; Libby et al. 2002). Clinical use of the proposed LSME imaging method to determine SSE may thus allow monitoring of the state of atherosclerotic plaque evolution and its response to therapies. This may help in decisions on timely interventions to prevent myocardial infarctions and strokes.

4. Finally, once clinically validated, the proposed method may allow the comparison of different patients with different atherosclerotic plaque properties or the same patient between different follow-ups. In this regard, SSE may be a useful quantity in monitoring the level of plaque vulnerability. Therefore, the proposed method may be helpful in confirming whether an intervention has been useful in stabilizing a vulnerable plaque.

Limitations

This study was performed on a small population because of the high cost associated with each pig experiment. Nevertheless, this study did reveal the advantages of SSE and how it is connected to plaque vulnerability. Other studies with less expensive animal models on larger populations and, preferably, an extension to human plaques are required to confirm our results. Furthermore, because inflammation is a major determinant in the detection of vulnerable plaques (Naghavi et al., 2003), future studies should also be dedicated to assessing the correlation between SSE maps and inflammation status. Finally, it should be noted that the thick vessel walls in some histology images may have been caused by incomplete fixation of the elastic recoil.

REFERENCES

Allen JD, Ham KL, Dumont DM, Sileshi B, Trahey GE, Dahl JJ. The development and potential of acoustic radiation force impulse (ARFI) imaging for carotid artery plaque characterization. Vasc Med 2011;16:302–311.

Ambrose JA, Tannenbaum MA, Alexopoulos D, Hjemdahl-Monsen CE, Leavy J, Weiss M, Borrico S, Corlin R, Fuster V. Angiographic progression of coronary artery disease and the development of myocardial infarction. J Am Coll Cardiol 1998;12:56–62.

Baldewsing RA, Danilouchkine MG, Mastik F, Schaar JA, Serruys PW, van der Steen AF. An inverse method for imaging the local elasticity of atherosclerotic coronary plaques. IEEE Trans Inf Technol Biomed 2008;12:277–289.

Baldewsing RA, de Korte CL, Schaar JA, Mastik F, van der Steen AF. Finite element modeling and intravascular ultrasound elastography of vulnerable plaques: Parameter variation. Ultrasonics 2004;42:723–729.

Briley-Saebo KC, Mulder WJ, Mani V, Hyafil F, Amirbekian V, Aguinaldo JG, Fisher EA, Fayad ZA. Magnetic resonance imaging of vulnerable atherosclerotic plaques: Current imaging strategies and molecular imaging probes. J Magn Reson Imaging 2007;26:460–479.

Brugaletta S, Garcia-Garcia HM, Serruys PW, Maehara A, Farooq V, Mintz GS, de Bruyne B, Marso SP, Verheye S, Dudek D, Hamm CW, Farhat N, Schiele F, McPherson J, Lerman A, Moreno PR, Wennerblom B, Fahy M, Templin B, Morel MA, van Es GA, Stone GW. Relationship between palpography and virtual histology in patients with acute coronary syndromes. JACC Cardiovasc Imaging 2012;5:19–27.

Carlier SG, Tanaka K. Studying coronary plaque regression with IVUS: A critical review of recent studies. J Interv Cardiol 2006;19:11–15.

Céspedes EI, de Korte CL, van der Steen AFW. Intraluminal ultrasonic palpation: Assessment of local and cross-sectional tissue stiffness. Ultrasound Med Biol 2000;26:385–396.

Cheng GC, Loree HM, Kamm RD, Fishbein MC, Lee RT. Distribution of circumferential stress in ruptured and stable atherosclerotic lesions: A structural analysis with histopathological correlation. Circulation 1993;87:1179–1187.

Cinthio M, Ahlgren AR, Bergkvist J, Jansson T, Persson HW, Lindstrom K. Longitudinal movements and resulting shear strain of the arterial wall. Am J Physiol Heart Circ Physiol 2006;291:394–402.

De Korte CL, Cespedes EI, van der Steen AFW. Influence of catheter position on estimated strain in intravascular elastography. IEEE Trans Ultrason Ferroelectr Freq Control 1999;46:616–625.

De Korte CL, Pasterkamp G, van der Steen AFW, Woutman HA, Bom N. Characterization of plaque components with intravascular ultrasound elastography in human femoral and coronary arteries *in vitro*. Circulation 2000;102:617–623.

De Korte CL, Sierevogel MJ, Mastik F, Strijder C, Schaar JA, Velema E, Pasterkamp G, Serruys PW, van der Steen AF. Identification of atherosclerotic plaque components with intravascular ultrasound elastography *in vivo*: A Yucatan pig study. Circulation 2002;105:1627–1630.

De Korte CL, van der Steen AF, Céspedes EI, Pasterkamp G. Intravascular ultrasound elastography in human arteries: Initial experience *in vitro*. Ultrasound Med Biol 1998;24:401–408.

Dickson BC, Gotlieb AI. Towards understanding acute destabilization of vulnerable atherosclerotic plaques. Cardiovasc Pathol 2003;12:237–248.

Falk E, Shah PK, Fuster V. Coronary plaque disruption. Circulation 1995;92:657–671.

Fayad ZA, Fuster V, Nikolaou K, Becker C. Computed tomography and magnetic resonance imaging for noninvasive coronary angiography and plaque imaging: Current and potential future concepts. Circulation 2002;106:2026–2034.

Finet G, Ohayon J, Rioufol G. Biomechanical interaction between cap thickness, lipid core composition and blood pressure in vulnerable coronary plaque: Impact on stability or instability. Coronary Artery Dis 2004;15:13–20.

Frutkin AD, Mehta SK, McCrary JR, Marso SP. Limitations to the use of virtual histology-intravascular ultrasound to detect vulnerable plaque. Eur Heart J 2007;28:1783–1784.

Fuster V, Moreno PR, Fayad ZA, Corit R, Badimon JJ. Atherothrombosis and high-risk plaque: Part I. Evolving concepts. J Am Coll Cardiol 2005;46:937–954.

Idzenga T, Holewijn S, Hansen HHG, de Korte CL. Estimating cyclic shear strain in the common carotid artery using radiofrequency ultrasound. Ultrasound Med Biol 2012;38:2229–2237.

Idzenga T, Pasterkamp G, de Korte CL. Shear strain in the adventitial layer of the arterial wall facilitates development of vulnerable plaques. Biosci Hypoth 2009;2:339–342.

Ishii A, Vinuela F, Murayama Y, Yuki I, Nien YL, Yeh DT, Vinters HV. Swine model of carotid artery atherosclerosis: Experimental induction by surgical partial ligation and dietary hypercholesterolemia. Am J Neuroradiol 2006;27:1893–1899.

Jang IK, Bouma BE, Kang DH, Park SJ, Park SW, Seung KB, Choi KB, Shishkov M, Schlendorf K, Pomerantsev E, Houser SL, Aretz HT, Tearney GJ. Visualization of coronary atherosclerotic plaques in patients using optical coherence tomography: Comparison with intravascular ultrasound. J Am Coll Cardiol 2002;39:604–609.

Lawrence-Brown M, Stanley BM, Sun Z, Semmens JB, Liffman K. Stress and strain behaviour modelling of the carotid bifurcation. ANZ J Surg 2011;81:810–816.

Le Floc'h S, Ohayon J, Tracqui P, Finet G, Gharib A, Maurice RL, Cloutier G, Pettigrew RI. Vulnerable atherosclerotic plaque elasticity reconstruction based on a segmentation-driven optimization procedure using strain measurements: Theoretical framework. IEEE Trans. Med. Imaging 2009;28:1126–1137.

Le Floc'h S, Cloutier G, Finet G, Tracqui P, Pettigrew RI, Ohayon J. On the potential of a new IVUS elasticity modulus imaging approach for detecting vulnerable atherosclerotic coronary plaques: *In vitro* vessel phantom study. Phys Med Biol 2010;55:5701–5721.

Liang Y, Zhu H, Friedman MH. Estimation of the transverse strain tensor in the arterial wall using IVUS image registration. Ultrasound Med Biol 2008;34:1832–1845.

Libby P. Current concepts of the pathogenesis of the acute coronary syndromes. Circulation 2001;104:365–372.

Libby P, Ridker PM, Maseri A. Inflammation and atherosclerosis. Circulation 2002;105:1135–1143.

Loree HM, Kamm RD, Stringfellow RG, Lee RT. Effects of fibrous cap thickness on peak circumferential stress in model atherosclerotic vessels. Circ Res 1992;71:850–858.

Maehara A, Cristea E, Mintz GS, Lansky AJ, Dressler O, Biro S, Templin B, Virmani R, de Bruyne B, Serruys PW, Stone GW. Definitions and methodology for the grayscale and radiofrequency intravascular ultrasound and coronary angiographic analyses. J Am Coll Cardiol Cardiovasc Imaging 2012;5:1–9.

Maurice RL, Fromageau J, Brusseau E, Finet G, Rioufol G, Cloutier G. On the potential of the Lagrangian estimator for endovascular ultrasound elastography: *In vivo* human coronary artery study. Ultrasound Med Biol 2007;33:1199–1205.

Maurice RL, Fromageau J, Roy Cardinal MH, Doyley M, de Muinck E, Robb J, Cloutier G. Characterization of atherosclerotic plaques and mural thrombi with intravascular ultrasound elastography: A potential method evaluated in an aortic rabbit model and a human coronary artery. IEEE Trans Inf Technol Biomed 2008;12:290–298.

Maurice RL, Ohayon J, Finet G, Cloutier G. Adapting the Lagrangian speckle model estimator for endovascular elastography: Theory and validation with simulated radio-frequency data. J Acoust Soc Am 2004;116:1276–1286.

Maurice RL, Ohayon J, Stoyanova E, Foster FS, Cloutier G. Non-invasive high-frequency vascular ultrasound elastography. Phys Med Biol 2005;50:1611–1628.

Murray SW, Stables RH, Hart G, Palmer ND. Defining the magnitude of measurement variability in the virtual histology analysis of acute coronary syndrome plaques. Eur Heart J Cardiovasc Imaging 2013;14:167–174.

Naghavi M, Libby P, Falk E, Casscells W, Litovsky S, Rumberger J, Badimon JJ, Stefanadis C, Moreno P, Pasterkamp G, Fayad Z, Stone PN, Waxman S, Raggi P, Madjid M, Zarrabi A, Burke A, Yuan C, Fitzgerald PJ, Siscovick DS, de Korte CL, Aikawa M, Airaksinen J, Assmann G, Becker CR, Chesebro JH, Farb A, Galis ZS, Jackson C, Jang IK, Koenig W, Lodder RA, March K, Demirovic J, Navab M, Priori SG, Rekhter MD, Bahr R, Grundy SM, Mehran R, Colombo A, Boerwinkle E, Ballantyne C, Insull W, Schwartz RS, Vogel R, Serruys PW, Hansson GK, Faxon DP, Kaul S, Drexler H, Greenland P, Muller JE, Virmani R, Ridker PM, Zipes DP, Shah PK, Willerson JT. From vulnerable plaque to vulnerable patient: A call for new definition and risk assessment strategies: Part I. Circulation 2003;108:1664–1672.

Nair A, Kuban BD, Tuzcu EM, Schoenhagen P, Nissen SE, Vince DG. Coronary plaque classification with intravascular ultrasound radiofrequency data analysis. Circulation 2002;106: 2200–2206.

Nair A, Margolis MP, Kuban BD, Vince DG. Automated coronary plaque characterization with intravascular ultrasound backscatter: *Ex vivo* validation. EuroIntervention 2007;3:113–120.

Ohayon J, Finet G, Gharib AM, Herzka DA, Tracqui P, Héroux J, Rioufol G, Kotys MS, Elagha A, Pettigrew RI. Necrotic core thickness and positive arterial remodeling index: Emergent biomechanical factors for evaluating the risk of plaque rupture. Am J Physiol Heart Circ Physiol 2008;295:717–727.

Perrey C, Wilkening W, Brendel B. A modified synthetic aperture focusing technique for the correction of geometric artefacts in intravascular ultrasound elastography. In: Proceedings, 2001 International IEEE Ultrasonics Symposium, Atlanta, Georgia, 7–10 October. New York: IEEE, 2001;2:1585–1588.

Redgrave JNE, Lovett JK, Gallagher PJ, Rothwell PM. Histological assessment of 526 symptomatic carotid plaques in relation to the nature and timing of ischemic symptoms: The Oxford Plaque Study. Circulation 2006;113:2320–2328.

Richards MS, Doyley MM. Investigating the impact of spatial priors on the performance of model-based IVUS elastography. Phys Med Biol 2011;56:7223–7246.

Rioufol G, Finet G, Ginon I, Andre-Fouet X, Rossi R, Vialle E, Desjoyaux E, Convert G, Huret JF, Tabib A. Multiple atherosclerotic plaque rupture in acute coronary syndrome: A three-vessel intravascular ultrasound study. Circulation 2002;106: 804–808.

Roy Cardinal MH, Meunier J, Soulez G, Maurice RL, Therasse E, Cloutier G. Intravascular ultrasound image segmentation: A three dimensional fast-marching method based on gray level distributions. IEEE Trans Med Imaging 2006;25:590–601.

Schaar JA, van der Steen AF, Mastik F, Baldewsing RA, Serruys PW. Intravascular palpography for vulnerable plaque assessment. J Am Coll Cardiol 2006;18:86–91.

Serruys PW, Garcia-Garcia HM, Buszman P, Erne P, Verheye S, Aschermann M, Duckers H, Bleie O, Dudek D, Botker HE, von Bigelen C, D'Amico D, Hutchinson T, Zambanini A, Mastik F, van Es GA, van der Steen AFW, Vince DG, Ganz P, Hamm CW, Wjns W, Zalewski A, for the Integrated Biomarker and Imaging Study-2 Investigators. Effects of the direct lipoprotein-associated phospholipase A(2) inhibitor darapladib on human coronary atherosclerotic plaque. Circulation 2008; 118:1172–1182.

Shapo BM, Crowe JR, Erkamp R, Emelianov SY, Eberle MJ, O'Donnell M. Strain imaging of coronary arteries with intraluminal ultrasound: Experiments on an inhomogeneous phantom. Ultrason Imaging 1996;18:173–191.

Shi H, Chen Q, Varghese T. A general solution for catheter position effects for strain estimation in intravascular elastography. Ultrasound Med Biol 2005;31:1509–1526.

Shi H, Varghese T, Chen Q, Gimelli G. Correction for simultaneous catheter eccentricity and tilt in intravascular elastography. Ultrason Imaging 2003;25:262–283.

Soulez G, Lerouge S, Allard L, Roméo P, Qi S, Héon H, Tardif JC, Cloutier G. Vulnerable carotid atherosclerotic plaque creation in a swine model: Evaluation of stenosis creation using absorbable and permanent suture in a diabetic dyslipidemic model. J. Vasc Interv Radiol 2012;23:1700–1708.

Stary HC. Natural history and histological classification of atherosclerotic lesions: an update. Arterioscler Thromb Vasc Biol 2000;20: 1177–1178.

Tearney GJ, Waxman S, Shishkov M, Vakoc BJ, Suter MJ, Freilich MI, Desjardins AE, Oh WY, Bartlett LA, Rosenberg M, Bouma BE. Three-dimensional coronary artery microscopy by intracoronary optical frequency domain imaging. JACC Cardiovasc Imaging 2008;1: 752–761.

Thim T, Hagensen MK, Wallace-Bradley D, Granada JF, Kaluza GL, Drouet L, Paaske WP, Botker HE, Falk E. Unreliable assessment of necrotic core by virtual histology intravascular ultrasound in porcine coronary artery disease. Circ Cardiovasc Imaging 2010;3: 384–391.

Van Mieghem CA, McFadden EP, de Feyter PJ, Bruining N, Schaar JA, Mollet NR, Cademartiri F, Goedhard D, de Winter S, Granillo GR, Valgimigli M, Mastik F, van der Steen AF, van der Giessen WJ, Sianos G, Backx B, Morel MA, van Es GA, Zalewski A, Serruys PW. Noninvasive detection of subclinical coronary atherosclerosis coupled with assessment of changes in plaque characteristics using novel invasive imaging modalities: The Integrated Biomarker and Imaging Study (IBIS). J Am Coll Cardiol 2006;47: 1134–1142.

Vengrenyuk Y, Carlier S, Xanthos S, Cardoso L, Ganatos P, Virmani R, Einav S, Gilchrist L, Weinbaum S. A hypothesis for vulnerable plaque rupture due to stress-induced debonding around cellular microcalcifications in thin fibrous caps. Proc Natl Acad Sci USA 2006; 103:14678–14683.

Virmani R, Burke AP, Farb A, Kolodgie FD. Pathology of the vulnerable plaque. J Am Coll Cardiol 2006;47:13–18.

Vito RP, Whang MC, Giddens DP, Zarins CK, Glagov S. Stress analysis of the diseased arterial cross-section. ASME Adv Bioeng Proc 1990; 19:273–276.

Wan M, Li Y, Li J, Cui Y, Zhou X. Strain imaging and elasticity reconstruction of arteries based on intravascular ultrasound video images. IEEE Trans Biomed Eng 2001;48:116–120.

APPENDIX A: ELASTOGRAPHY ALGORITHM

Because our aim was to find components of the strain tensor within the artery wall, displacements at any location as well as their spatial derivatives were required. For this purpose, the LSME developed in the context of EVE was adapted to process IVUS-derived RF signals in the polar coordinate system.

First-order optical flow constraint equation

The LSME algorithm is based on the optical flow constraint equation (OFCE), which assumes that the signal intensity corresponding to each material point remains unchanged over time. This assumption is generally true whenever the signal acquisition conditions are not changed from one frame to the next and tissue displacements are small. The OFCE can be written using the material derivative of the intensity signal I as

$$\frac{DI}{Dt} = 0 \tag{A1}$$

where t refers to time. For a specific spatial point P_i, eqn (A1) can be rewritten as

$$\frac{\partial I}{\partial t}(P_i, t) + \vec{v}(P_i, t) \cdot \vec{\nabla} I(P_i, t) = 0, \tag{A2}$$

where the nabla operator ∇ stands for the gradient. This equation results in an under-determined system of equations. To overcome this problem, the first-order Taylor series expansion about a given point M_0 is used. The speckle velocity $\vec{v}$ at point P_i can then be expanded as

$$\vec{v}(P_i, t) = \vec{v}(M_0, t) + [\overline{\overline{\nabla}} \vec{v}]_{(M_0,t)} \overrightarrow{M_0 P_i}. \qquad (A3)$$

Inserting expression (A3) into (A2) leads to the first-order OFCE for any point P_i surrounding M_0:

$$\frac{\partial I}{\partial t}(P_i, t) + \left\{ \vec{v}(M_0, t) + [\overline{\overline{\nabla}} \vec{v}]_{(M_0,t)} \overrightarrow{M_0 P_i} \right\} \cdot \vec{\nabla} I(P_i, t) = 0. \qquad (A4)$$

The OFCE in polar coordinates

In clinical practice, RF signals generated by IVUS scanners are formatted in a polar coordinate system centered on the catheter center C. Let $\{C, \vec{e}_r, \vec{e}_\theta\}$ denote the associated physical basis and (r, θ) the corresponding polar coordinates. Under these conditions, the expressions obtained are

$$\vec{v}(M_0, t) = v_{r_0} \vec{e}_r(M_0) + v_{\theta_0} \vec{e}_\theta(M_0);$$

$$[\overline{\overline{\nabla}} \vec{v}]_{(M_0,t)} = \begin{bmatrix} \frac{\partial v_r}{\partial r} & \frac{1}{r}\left(\frac{\partial v_r}{\partial \theta} - v_\theta\right) \\ \frac{\partial v_\theta}{\partial r} & \frac{1}{r}\left(\frac{\partial v_\theta}{\partial \theta} + v_r\right) \end{bmatrix}_{(r_0, \theta_0)};$$

$$\overrightarrow{M_0 P_i} = (r_i \cos(\theta_i - \theta_0) - r_0)\vec{e}_r(M_0) + r_i \sin(\theta_i - \theta_0)\vec{e}_\theta(M_0); \qquad (A5)$$

$$\vec{\nabla} I(P_i, t) = \frac{\partial I}{\partial r}(r_i, \theta_i, t)\vec{e}_r(P_i) + \frac{1}{r_i}\frac{\partial I}{\partial \theta}(r_i, \theta_i, t)\vec{e}_\theta(P_i)$$

$$= \left(\cos(\theta_i - \theta_0)\frac{\partial I}{\partial r}(r_i, \theta_i, t) - \sin(\theta_i - \theta_0)\frac{1}{r_i}\frac{\partial I}{\partial \theta}(r_i, \theta_i, t)\right)\vec{e}_r(M_0)$$

$$+ \left(\sin(\theta_i - \theta_0)\frac{\partial I}{\partial r}(r_i, \theta_i, t) + \cos(\theta_i - \theta_0)\frac{1}{r_i}\frac{\partial I}{\partial \theta}(r_i, \theta_i, t)\right)\vec{e}_\theta(M_0).$$

Substituting all components of eqn (A5) into eqn (A4) yields the first-order OFCE for any point P_i (r_i, θ_i) surrounding M_0 (r_0, θ_0) in the polar system $\{C, \vec{e}_r(M_0), \vec{e}_\theta(M_0)\}$.

The LSME in polar coordinates

The first-order OFCE is a scalar equation that contains six unknowns at M_0 (i.e., v_{r0} and $v_{\theta0}$ and their respective spatial derivatives $\partial v_r/\partial r$; $\partial v_r/\partial \theta$, $\partial v_\theta/\partial r$ and $\partial v_\theta/\partial \theta$). The LSME now consists of solving such a first-order OFCE equation within a small ROI surrounding a given point M_0: the OFCE is written at each point P_i ($i = 1, \ldots, n$, with $n > 6$) of the ROI. This leads to an over-determined system, which is solved in the least-squares sense. Thus, for a given ROI centered at M_0, components of the strain tensor are expressed as

$$\varepsilon_{rr} = \frac{\partial u_r}{\partial r}; \; \varepsilon_{\theta\theta} = \frac{1}{r}\left(\frac{\partial u_\theta}{\partial \theta} + u_r\right); \; \varepsilon_{r\theta} = \frac{1}{2}(\Delta_{r\theta} + \Delta_{\theta r}); \qquad (A6)$$

$$\Delta_{r\theta} = \frac{1}{r}\left(\frac{\partial u_r}{\partial_\theta} - u_\theta\right); \; \Delta_{\theta r} = \frac{\partial u_\theta}{\partial r},$$

where $u_r = v_r \Delta t$ and $u_\theta = v_\theta \Delta t$ are displacements, and Δt is the elapsed time between two consecutive IVUS RF frames. Readers can refer to Maurice et al. (2004) on how to compute each component of the displacement gradient matrix based on an over-determined system. In the present study, we investigated only one component (first term of $\Delta_{r\theta}$ in eqn [A6]) of the shear strain, referred to as the shear strain component or SSE map.

APPENDIX B: COMPENSATION OF THE ECCENTRICITY OF THE CATHETER

With IVUS imaging, the catheter position is often eccentric with respect to the vessel lumen, as schematically visualized in Figure A1. If the probe position is eccentric, the resulting B-mode or RF-mode image will still be geometrically correct, but subsequent strain estimates will be biased.
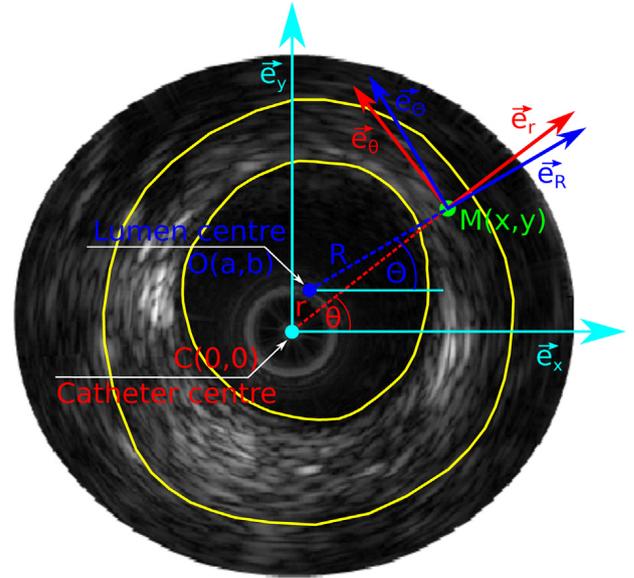
Fig. A1. Schematic of intravascular ultrasound segmentation and compensation of catheter eccentricity. This scheme handles general geometric shapes; therefore, its use is not restricted to circular geometries.

With knowledge of this catheter position (center of the image), errors can be corrected, as described below, by computations originating from the lumen center rather than from the catheter center. To determine the center of the luminal cavity, the lumen contour was found by a segmentation of B-mode images (Roy Cardinal et al. 2006). The center of gravity $O(a, b)$ of the luminal border points constitutes its center. The Cartesian coordinate system is centered on the middle of the catheter C (Fig. A1). For the mathematical formulation given next, the Cartesian and polar unit base vectors and their associated physical coordinates are noted: $(O, \vec{e}_x, \vec{e}_y)$, $(O, \vec{e}_R, \vec{e}_\Theta)$ and $(C, \vec{e}_r, \vec{e}_\theta)$, respectively (Fig. A1).

The relation between the gradient in Cartesian and polar coordinates, using the lumen center as the origin of the system $(O, \vec{e}_R, \vec{e}_\Theta)$ and the middle of the catheter as the origin of the other system $(C, \vec{e}_r, \vec{e}_\theta)$, is expressed as

$$[\overline{\overline{\nabla}} \vec{u}]_{R,\Theta} = [P]^{-1}[\overline{\overline{\nabla}} \vec{u}]_{x,y}[P] \qquad (A7)$$

$$[\overline{\overline{\nabla}} \vec{u}]_{x,y} = [P^*][\overline{\overline{\nabla}} \vec{u}]_{r,\theta}[P^*]^{-1} \qquad (A8)$$

where matrices P and P^*, the angle Θ and the radius R are given as

$$[P] = \begin{bmatrix} \cos\Theta & \sin\Theta \\ -\sin\Theta & \cos\Theta \end{bmatrix}; \; [P^*] = \begin{bmatrix} \cos\theta & \sin\theta \\ -\sin\theta & \cos\theta \end{bmatrix};$$

$$\Theta = \tan^{-1}\left[\frac{(y-b)}{(x-a)}\right]; \; R = \sqrt{(x-a)^2 + (y-b)^2} \qquad (A9)$$

By substituting all components of eqn (A8) into eqn (A7), it is possible to determine the relation between the gradient in polar coordinates $(O, \vec{e}_R, \vec{e}_\Theta)$ and $(C, \vec{e}_r, \vec{e}_\theta)$.

$$[\overline{\overline{\nabla}} \vec{u}]_{R,\Theta} = [P]^{-1}[\overline{\overline{\nabla}} \vec{u}]_{x,y}[P]$$
$$= [P]^{-1}[P^*][\overline{\overline{\nabla}} \vec{u}]_{r,\theta}[P^*]^{-1}[P] \qquad (A10)$$

By considering the matrix $[Q]$ defined as

$$[Q]^{-1} = [P]^{-1}[P^*] = \begin{bmatrix} \overline{C} & \overline{S} \\ -\overline{S} & \overline{C} \end{bmatrix} \qquad \text{(A11)}$$

or

$$[Q] = [P^*]^{-1}[P] = \begin{bmatrix} \overline{C} & -\overline{S} \\ \overline{S} & \overline{C} \end{bmatrix}$$

where $\overline{C}$ and $\overline{S}$ are $\cos(\Theta-\theta)$ and $\sin(\Theta-\theta)$, respectively, provides the transformation between the two polar systems:

$$\left[\overline{\overline{\nabla u}}\right]_{R,\Theta} = [Q]^{-1}\left[\overline{\overline{\nabla u}}\right]_{r,\theta}[Q] \qquad \text{(A12)}$$

Also, the displacement gradient tensor in the physical basis $(O, \vec{e}_R, \vec{e}_\Theta)$ according to the physical basis $(C, \vec{e}_r, \vec{e}_\theta)$ can be rewritten as

$$\begin{bmatrix} \Delta_{RR} & \Delta_{R\Theta} \\ \Delta_{R\Theta} & \Delta_{\Theta\Theta} \end{bmatrix}_{(\vec{e}_R, \vec{e}_\Theta)} = \begin{bmatrix} \overline{C} & \overline{S} \\ -\overline{S} & \overline{C} \end{bmatrix} \begin{bmatrix} \Delta_{rr} & \Delta_{\theta r} \\ \Delta_{r\theta} & \Delta_{\theta\theta} \end{bmatrix}_{(\vec{e}_r, \vec{e}_\theta)} \begin{bmatrix} \overline{C} & -\overline{S} \\ \overline{S} & \overline{C} \end{bmatrix} \qquad \text{(A13)}$$

or

$$\begin{cases} \varepsilon_{RR} = \Delta_{RR} = \varepsilon_{rr}\overline{C}^2 + 2\varepsilon_{r\theta}\overline{CS} + \varepsilon_{\theta\theta}\overline{S}^2 \\ \varepsilon_{\Theta\Theta} = \Delta_{\Theta\Theta} = \varepsilon_{rr}\overline{S}^2 - 2\varepsilon_{r\theta}\overline{CS} + \varepsilon_{\theta\theta}\overline{C}^2 \\ \Delta_{R\Theta} = -\varepsilon_{rr}\overline{CS} - \Delta_{\theta r}\overline{S}^2 + \Delta_{r\theta}\overline{C}^2 + \varepsilon_{\theta\theta}\overline{CS} \\ \varDelta_{\Theta R} = -\varepsilon_{rr}\overline{CS} + \varDelta_{\theta r}\overline{C}^2 + \varDelta_{r\theta}\overline{S}^2 + \varepsilon_{\theta\theta}\overline{CS} \\ \varepsilon_{R\Theta} = \frac{1}{2}(\Delta_{R\Theta} + \Delta_{\Theta R}) = -\varepsilon_{rr}\overline{CS} + \varepsilon_{r\theta}\left(\overline{C}^2 - \overline{S}^2\right) + \varepsilon_{\theta\theta}\overline{CS} \end{cases} \qquad \text{(A14)}$$

Note that the general formulations developed in Appendices A and B are based on a geometric transformation between Cartesian and polar coordinates; no assumption on the shape of the vessels is required (not necessarily circular).